

# A computationally-enhanced hiCLIP atlas reveals Staufen1-RNA binding features and links 3' UTR structure to RNA metabolism

Anob M. Chakrabarti <sup>1,\*</sup>, Ira A. Iosub <sup>1</sup>, Flora C.Y. Lee <sup>1,2</sup>, Jernej Ule <sup>1,2,3</sup> and Nicholas M. Luscombe <sup>1,4</sup>

<sup>1</sup>The Francis Crick Institute, London, NW1 4AT, UK, <sup>2</sup>Department of Neuromuscular Diseases, UCL Queen Square Institute of Neurology, London, WC1N 3BG, UK, <sup>3</sup>UK Dementia Research Institute at King's College London, Institute of Psychiatry, Psychology and Neuroscience, London, SE5 9RX, UK and <sup>4</sup>Okinawa Institute of Science and Technology Graduate University, Onna-son, Okinawa 904-0495, Japan

Received June 15, 2022; Revised February 08, 2023; Editorial Decision March 06, 2023; Accepted March 31, 2023

## ABSTRACT

The structure of mRNA molecules plays an important role in its interactions with *trans*-acting factors, notably RNA binding proteins (RBPs), thus contributing to the functional consequences of this interplay. However, current transcriptome-wide experimental methods to chart these interactions are limited by their poor sensitivity. Here we extend the hiCLIP atlas of duplexes bound by Staufen1 (STAU1) ~10-fold, through careful consideration of experimental assumptions, and the development of bespoke computational methods which we apply to existing data. We present *Tosca*, a Nextflow computational pipeline for the processing, analysis and visualisation of proximity ligation sequencing data generally. We use our extended duplex atlas to discover insights into the RNA selectivity of STAU1, revealing the importance of structural symmetry and duplex-span-dependent nucleotide composition. Furthermore, we identify heterogeneity in the relationship between transcripts with STAU1-bound 3' UTR duplexes and metabolism of the associated RNAs that we relate to RNA structure: transcripts with short-range proximal 3' UTR duplexes have high degradation rates, but those with long-range duplexes have low rates. Overall, our work enables the integrative analysis of proximity ligation data delivering insights into specific features and effects of RBP-RNA structure interactions.

## INTRODUCTION

Interactions between RNA and associated *trans*-acting factors, notably RNA binding proteins (RBPs), are important for post-transcriptional regulation. It is becoming in-

creasingly evident that the structure of RNA molecules plays an important role in this interplay. In particular, there are RBPs that contain protein domains that specifically bind double-stranded RNA (dsRNA) duplexes. The Staufen family is one such group of proteins with important roles in mRNA localisation, stability and translation. In order to understand the relationships between RNA structure, Staufen binding and the functional consequences, a comprehensive transcriptome-wide atlas of the bound structures *in vivo* is needed.

To this end, hiCLIP (hybrid individual-nucleotide resolution UV crosslinking and immunoprecipitation), an RNA proximity ligation method (Figure 1A) was developed to study RNA duplexes bound by double-stranded RNA binding proteins (dsRBPs), such as Staufen1 (STAU1) (1,2). UV-C is used to crosslink RBP-RNA complexes *in vivo*, following which cells are lysed and RNA partially fragmented by RNase I. RBP-bound duplexes are enriched by immunoprecipitation, and the two fragments of interacting RNA strands ligated together. After digesting the bound RBP, cDNA is prepared from these molecules and sequenced. Two successfully ligated RNA fragments will yield a hybrid read, which we define as a sequencing read that maps non-contiguously to the transcriptome and thus represents two proximity ligated fragments (Figure 1A, purple and green panels). Hybrid reads represent a duplex, which we define as a *unique* RNA structure formed by two strands of RNA—thus a duplex detected by hiCLIP can be supported by multiple hybrids. We refer to each hybrid or duplex as having two arms: the proximal arm is the 5'-most and the distal arm the 3'-most, each corresponding to one ligated RNA fragment. The non-ligated RNAs, which constitute the rest of the library, yield non-hybrid reads, which we define as a sequencing read that maps contiguously to the transcriptome and represents one RNA fragment. These reads may or may not represent a duplex (Figure 1A, turquoise panel).

\*To whom correspondence should be addressed. Tel: +44 20 3796 0000; Email: [anob.chakrabarti@crick.ac.uk](mailto:anob.chakrabarti@crick.ac.uk)

Although proximity ligation experiments are primarily aimed at detecting hybrid reads, recovered hybrids typically constitute only a minority of the sequencing data due to both experimental and computational challenges: the ligation efficiency is low and accurate hybrid read identification and delineation of the original interacting RNA fragments is non-trivial. A data analysis challenge here is to determine unambiguously where the two arms start and end within sequencing reads, so that they can be mapped to the correct transcript locations. To address these issues, the hiCLIP method improved on previous methods (e.g. Crosslinking, Ligation And Sequencing of Hybrids; CLASH (3)), most notably by introducing a linker adapter to bridge the two RNA fragments into a single molecule instead of relying upon direct proximity ligation. This key innovation was devised to increase ligation efficiency (2) as well as streamline the computational workflow and ensure non-ambiguous assignment of the hybrid read arms to the correct transcriptomic loci. Therefore, the original computational pipeline searched for reads containing the linker adapter sequence flanked by the two arms. The two arms were individually mapped to the transcriptome, and then transcriptomic regions containing pairs of mapped arms originating from the same hybrid defined as duplex-forming. A drawback of this approach is that only 1–2% of all reads in the sequencing libraries were classified as hybrid (2). Ultimately, this meant that fewer than 1000 duplexes in the transcriptome could be confidently identified (i.e. with more than 1 supporting hybrid read). Given the low sensitivity of duplex detection, we hypothesise that only a fraction of the *in vivo* STAU1 duplexes have been recovered from the data.

Moreover, the paucity of robustly-detected duplexes limits the extent to which hiCLIP results can be broadly integrated with other transcriptome-wide RNA duplex datasets, such as PARIS (4), or functional RNA metabolism datasets, such as 4sU-seq (5) to contextualise the Staufen-bound duplexes and gain further biological insights. While a role for STAU1 in RNA metabolism has been established for selected transcripts and regulatory mechanisms have been described, such as polysome association (6) and Staufen mediated decay (7,8), a systematic transcriptome-wide exploration of the effect of STAU1-bound duplexes on RNA metabolism and stability has been lacking. Motivated to reveal the nature of STAU1 binding and its consequent effects on RNA metabolism on a transcriptome-wide scale, we aimed to improve hybrid detection from the STAU1 hiCLIP data—a prerequisite for more thorough investigations.

To improve the sensitivity of duplex detection from hiCLIP data, we refined and extended the computational approach. Specifically, we re-evaluated the experimental steps to understand where duplexes could potentially have been ‘lost’ in the original data analysis through misassignment of non-hybrid reads. We challenged three key assumptions of specific steps of the experimental protocol through which this could have occurred (Figure 1A).

First, we sought to recover hybrids containing truncated linker adapter sequences. 20–30% of the reads were found to contain linker-sequencing adapter dimers rather than sequencing adapters alone (2), suggesting that as the linker adapter is composed of ribonucleotides it is susceptible to

degradation. Thus, this raises the possibility that a few nucleotides may have been degraded from the 3′ end of linker adapters, however, these shorter linker adapters were originally not searched for in the hybrid read selection process.

Second, we assessed for the direct proximity ligation of duplex arms, resulting in hybrids lacking the linker adapter sequence. The original computational approach assumed that the vast majority of RNA hybrids contained the intermolecular linker due to the observed inefficiencies of circularisation and that sufficiently long stretches of single stranded RNA to enable circularisation would not remain after RNase digestion (2,9). Thus hybrids arising from direct proximity ligation were previously not considered. However, we know from CLASH (3,10) that intermolecular ligation can occur in many cases without a linker adapter. This has also been found in other subsequently developed proximity ligation methods (4,11,12). Hence, we hypothesised that there were a proportion of hiCLIP duplexes where the linker adapter failed to ligate (Figure 1A, green step 3), but were still subjected to the second ligation reaction (Figure 1A, step 5). In other words, direct proximity ligation of the two arms in the absence of a linker adapter was present in the hiCLIP data, provided the single-stranded overhangs were sufficiently long. However, such hybrid reads were assigned as non-hybrid in the original analysis as they would not contain the linker adapter.

Third, we identified short-range structures with undigested loops. RNase is used to digest the unprotected, primarily single-stranded RNA that connects the two duplex arms (Figure 1A, step 2). However, short loops between the two arms in a stem-loop may be inefficiently cleaved, partly due to being sterically protected by the RBP from the action of the RNase. Although such stem-loops are isolated by virtue of being crosslinked to STAU1, sequencing reads arising from them will map to the genome as a contiguous sequence and thus be assigned as non-hybrids.

In summary, we predict that there will be three types of sequencing read containing a bound RNA duplex (Figure 1A): (i) hybrid read with a linker adapter, either full-length or truncated (purple); (ii) hybrid read without a linker adapter containing a hybrid through direct proximity ligation (green); (iii) non-hybrid read, containing a duplex with a short-range loop (turquoise).

Here, we evaluate each of these hypotheses (Figure 1B) and in so doing present a Nextflow computational pipeline, *Tosca* (Supplementary Figure S1), for the processing and analysis of proximity ligation experiments. In refining our understanding of the consequences of particular experimental steps and by computationally addressing their alternative outcomes, we obtain a ~10-fold increase in identified duplexes from a previously published STAU1 hiCLIP dataset (Figure 2, Supplementary Figure S2 and Figure 3). In addition we develop a computational approach to study local RNA structures around sites of RBP binding, which can be applied generally to any RBP of interest (Figure 3). This extended set of STAU1 hiCLIP duplexes (Figure 4) enables us to contextualise STAU1-bound duplexes in the universe of global RNA structures (Figure 5) and furthermore, to derive insights into the relationship between STAU1 binding and RNA metabolism (Figure 6).

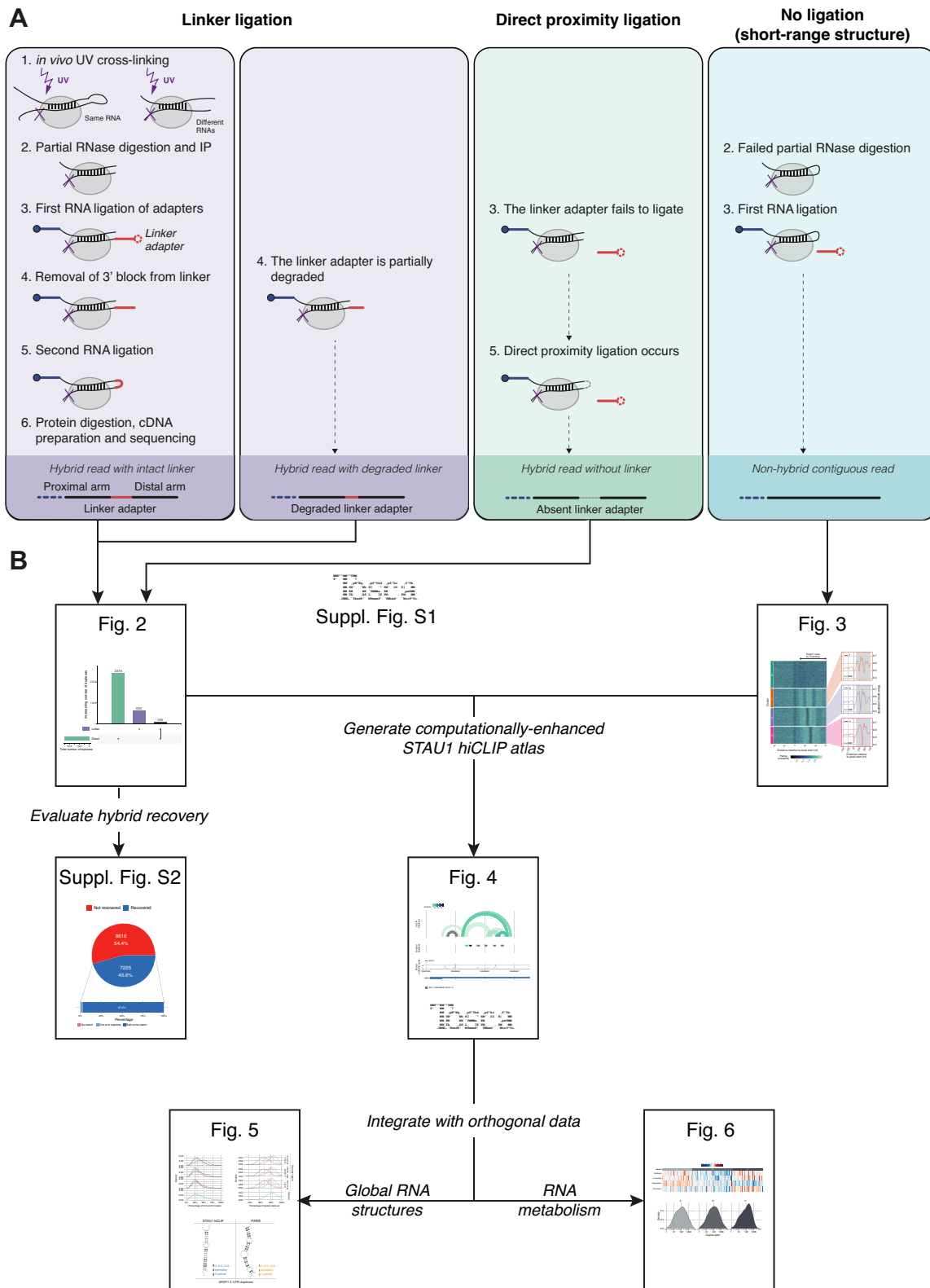


**Figure 1.** The hiCLIP method and sources of hybrid reads with a roadmap through the presented analysis and results. (A) Evaluation of the hiCLIP experimental steps to assess where in the data analysis duplexes could potentially have been 'lost' in the original analysis (2) and the corresponding types of reads in each scenario. (B) A roadmap through the analysis, initially computationally-extending the atlas, then generating integrative insights, with the corresponding figures indicated.

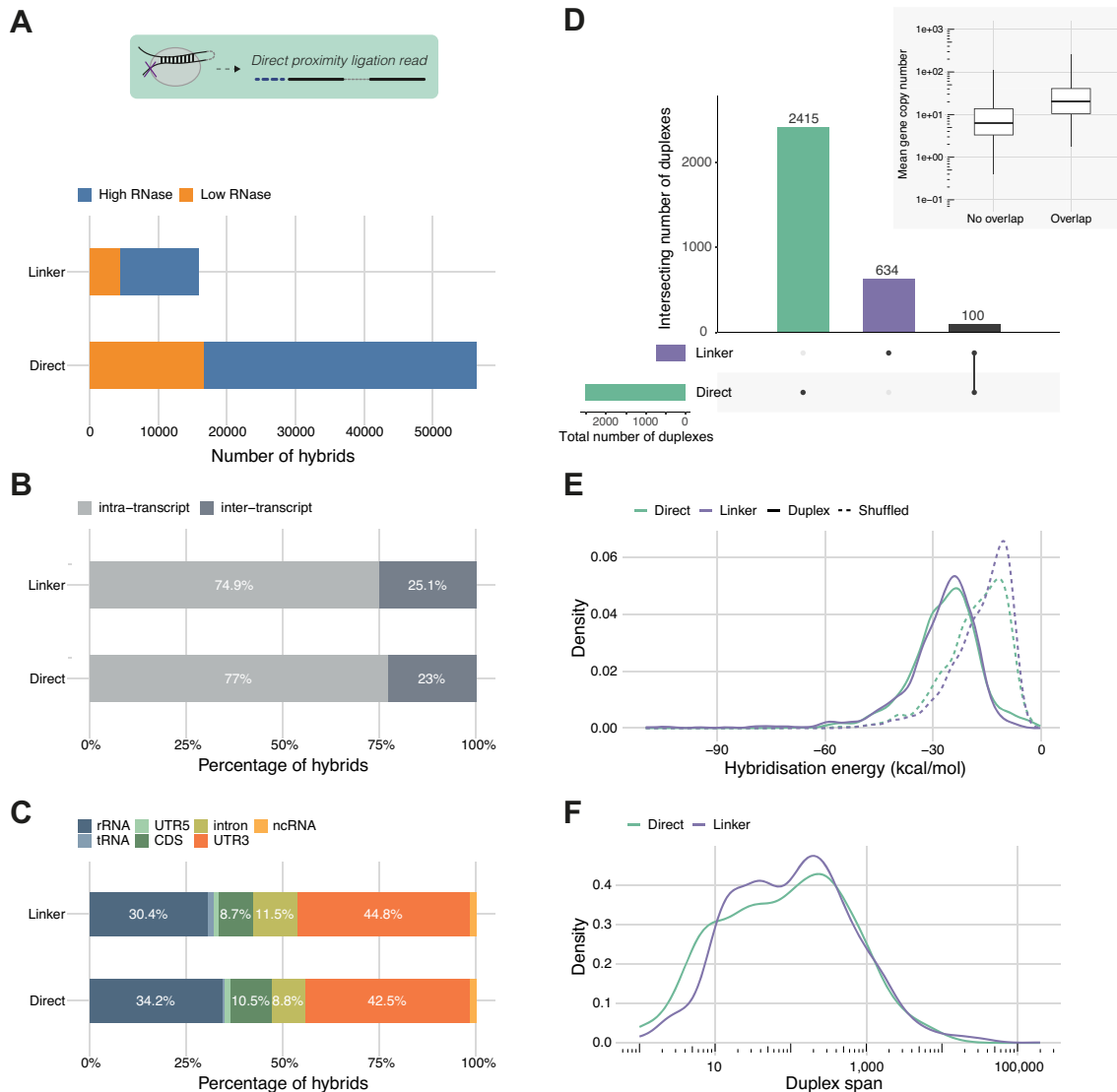


**Figure 2.** Direct proximity ligation is a major source of hybrid reads. (A) Comparison of hybrid counts across RNase concentration conditions for linker-containing hybrids and direct proximity ligation hybrids detected using *Tosca*. (B) Proportions of intra- and inter-transcript hybrids for the two hybrid read types (both RNase conditions pooled). (C) Regional distribution of hybrid arms for the two hybrid read types. (D) Overlap between confident duplexes derived from linker-containing hybrids and direct proximity ligation hybrids, respectively. Inset: gene expression of the genes on which duplexes were detected in both read types, compared with those in which duplexes were only detected in one. (E) Hybridisation energy of linker duplexes and direct proximity ligation duplexes compared to their corresponding shuffled controls. (F) Duplex spans (i.e. genomic distance between proximal and distal arms) of linker duplexes and direct proximity ligation duplexes.

## MATERIALS AND METHODS

### Data provenance

Raw STAU1 hiCLIP sequencing data from (2) was downloaded from ArrayExpress (E-MTAB-2937) and demultiplexed into the two RNase conditions (high and low). Three replicates of raw PARIS sequencing data in HEK293T cells were obtained from GEO (SRR2814763-5). Two replicates of raw rRNA-depleted RIC-seq data in HeLa cells were obtained from GEO (SRR8632820 and SRR8632821). For all experiments, each replicate was processed separately as described below.

### Reference annotation and sequence creation

For all analyses we used the GRCh38 build of the human genome with the Gencode V33 annotation. We created a custom reference sequence for the alignment of hybrid reads. This was necessary to reduce the complexity of the alignment problem for direct proximity ligation reads (i.e. without a linker adapter) to make it computationally tractable; largely by removing unannotated regions of the genome. We started to create this reference sequence by combining rDNA and 5S rRNA sequences from NCBI (U13369.1 and NR\_023363.1); mature tRNA sequences from gTRNAdb (13). We then selected genes

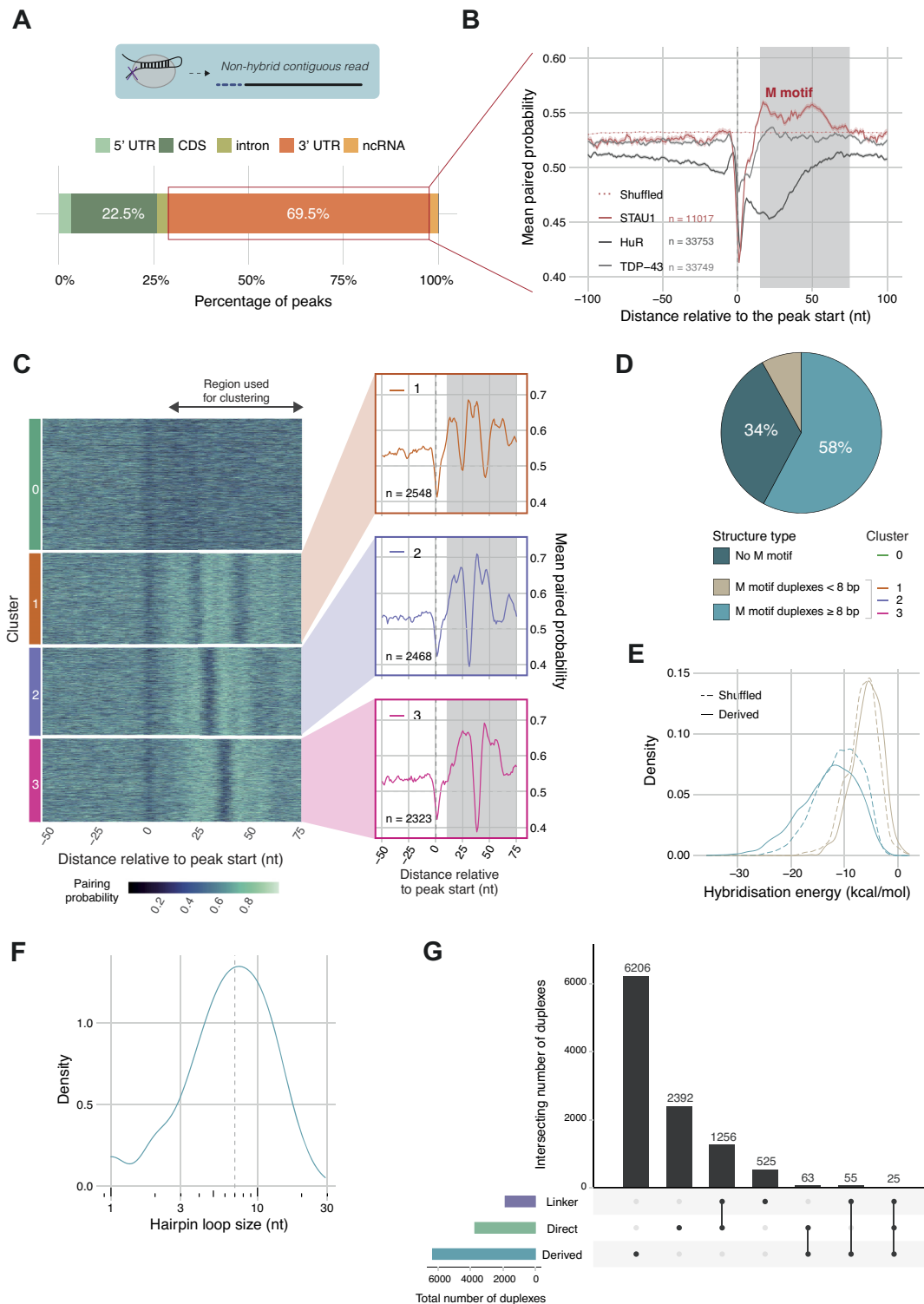


**Figure 3.** Deriving STAU1-bound short-range duplexes crosslinking peaks. **(A)** Regional distribution of STAU1 peaks from non-hybrid reads in STAU1 hiCLIP data. **(B)** Paired probability metaprofiles centred on peak starts for three RBPs known to bind to 3' UTRs (STAU1, HuR, TDP-43). For each RBP, the 3' UTRs with peaks specific to each RBP were used to construct the metaprofiles (STAU1—11 428 peaks, TDP-43—8301 peaks, HuR—33 753 peaks). The grey shaded area (+10 to +75 nt) indicates the relative area spanned by the 'M' shaped profile specific to STAU1. **(C)** Heatmap of clustered paired probability profiles for STAU1 3' UTR peaks. The clusters were generated by *k*-means clustering using the +10...+75 nt region relative to peak starts. On the right, the corresponding mean probability profiles for the three clusters with high paired probability downstream STAU1 (i.e. occurrence of 'M' shaped profile). **(D)** Proportion of peaks with or without predicted downstream duplexes and their classification based on the number of paired residues. **(E)** Hybridisation energy of the derived short-range duplexes compared to corresponding shuffled controls. **(F)** Hairpin loop size distribution for STAU1 derived stem-loop duplexes. **(G)** The final enhanced atlas of STAU1 hiCLIP duplexes comprising the full set of hybrids from proximity ligation (direct proximity ligation or via the linker) and 3' UTR derived structures. The number of duplexes supported by each or multiple sources is indicated.



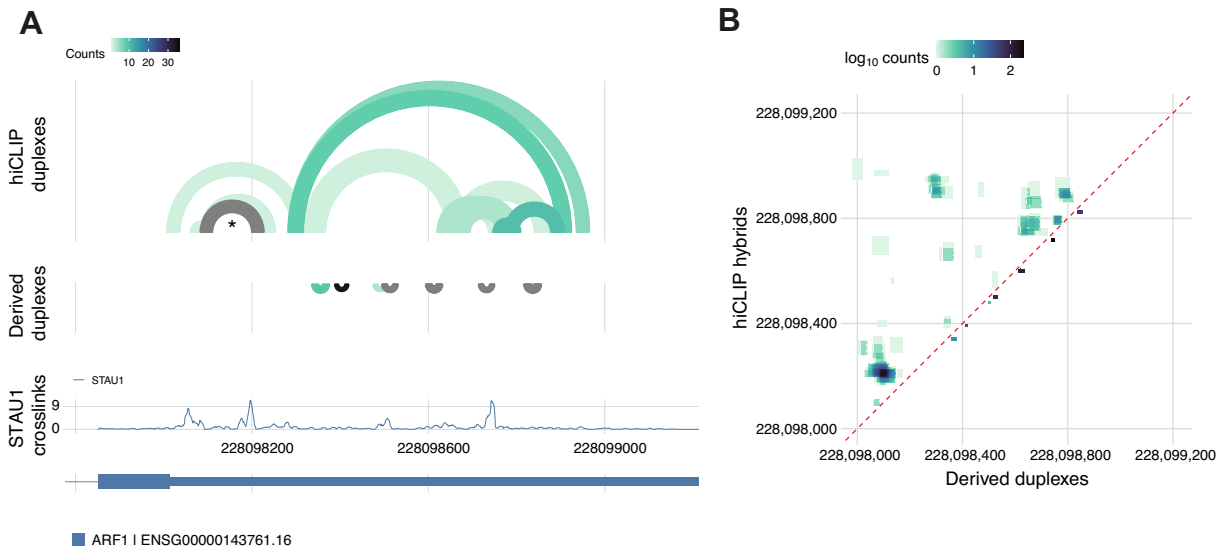


**Figure 4.** *Tosca* incorporates visualisation capabilities to integrate identified duplexes with other genomic datasets. (A) Arc plot of the experimental hiCLIP range and short-range derived duplexes on the *ARF1* 3' UTR (grey indicates counts >35), alongside STAU1 crosslinking signal and transcriptomic annotation; the known structure re-discovered in the STAU1 hiCLIP data is marked with an asterisk. (B) Contact map matrix showing counts at each base pairing location with experimental hiCLIP duplexes above the diagonal (dashed red line) and derived duplexes below.

annotated in Gencode V33 as: 'protein\_coding', 'IG\_[A-Z]\_gene' and 'TR\_[A-Z]\_gene' as protein coding genes and those annotated as 'lncRNA' or 'vault.RNA' as non-coding. We collapsed overlapping genes, concatenating the gene names, to avoid duplicating the same region in our reference sequence.

To obtain the corresponding sequences, first we created a mask that contained the genomic coordinates of regions: (i) annotated in Gencode V33 as: 'rRNA', 'rRNA\_pseudogene', or 'snRNA'; (ii) annotated in gRNAdb as tRNA; and (iii) annotated by RepeatMasker (obtained from the UCSC table browser) as: 'rRNA', 'tRNA', 'snRNA', 'srpRNA', 'scrRNA' or 'RNA' (the latter corresponding to 7SK). We used this as input to BEDtools (14) to mask the GRCh38 sequence before obtaining the sequences for each of our selected RNAs to create our reference.

To annotate the hybrid arms, duplex arms and crosslink sites uniquely, we used a flattened annotation produced by iCount-Mini (<https://github.com/ulelab/icount-mini>) and as previously detailed for iCLIP (15). However, given the very strong 3' UTR regional binding preference seen in the STAU1 data, we ranked 3' UTR regions over CDS when considering overlapping transcripts.

#### Identification and alignment of hybrids with a linker adapter

To identify duplexes from hybrid reads with a linker present we broadly followed the originally published method (1,2). As previously, we used Cutadapt (16) to trim the 3' sequencing adapters and linker and sequencing adapter concatemers. Then we identified reads containing the full-length linker adapter. We additionally examined the reads for truncated linker adapters missing either the last or the last two nucleotides. We kept reads for which there were at least 12 nt sequences flanking the linker adapter, splitting out the two as the two hybrid arms for alignment.

As it was not possible to perform the original iterative stepwise alignment (first to rRNA, then tRNA, then mRNA and ncRNA) for direct proximity ligation reads without a linker adapter, in order to ensure consistency we also aligned each hybrid arm in one step to our reference sequences using STAR v 2.7.7a (17).

To mimic direct proximity ligation (i.e. hybrid reads without a linker adapter) *in silico* for these reads which we knew contained hybrids, we stitched together the two hybrid arm sequences after removing the intervening linker adapter sequence.

#### *Tosca*: a nextflow pipeline for proximity ligation data analysis and visualisation

To analyse hybrid reads created through direct proximity ligation i.e. from sequencing reads without a linker adapter, we developed a computational analysis pipeline, *Tosca*, in Nextflow (18) (Supplementary Figure S1). *Tosca* first performs hybrid read identification, alignment and annotation; and duplex delineation using a graph-based clustering of hybrid read alignments, hybridisation energy calculation and generation of IGV tracks and plots for visualisation. The default parameter settings detailed below can all be optionally customised.

*Identification and alignment of hybrids created through direct proximity ligation.* Our proximity ligation hybrid read identification approach is inspired by the hyb pipeline (10) originally written for CLASH data. The basis of the method is to derive an optimal solution to the problem that a given sequencing read contains two sections that each align to two different parts of the reference, but that the location of the join between the two in the read sequence is unknown. As input to this stage of the analysis we use all reads in which a linker adapter (full-length or truncated) had not been de-

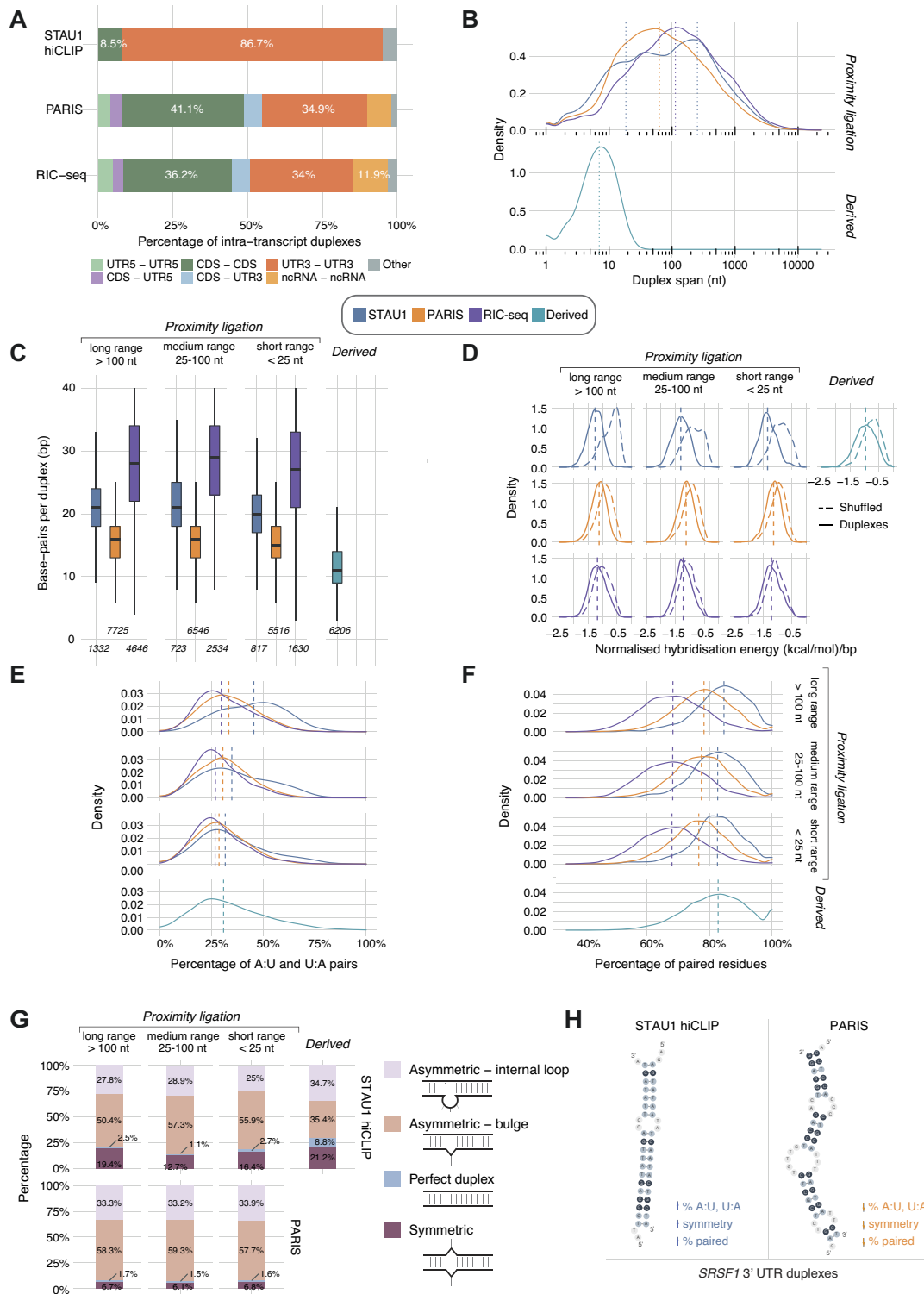


**Figure 5.** Contextualisation of STAU1 hiCLIP duplexes in the global universe of duplexes detected by PARIS and RIC-seq highlights features driving STAU1 RNA selectivity. (A) Regional distribution of intra-transcript pairwise interactions between proximity ligation STAU1 hiCLIP and PARIS duplexes and RIC-seq interactions. (rRNA, tRNA and intronic duplexes were excluded from this analysis.) (B) Spans of 3' UTR intra-transcript duplexes and interactions. (C) Number of paired residues within duplexes. (D) Normalised hybridisation energy of 3'UTR intra-transcript duplexes compared to shuffled controls. (E) A:U and U:A base-pair percentage distributions. (F) Percentage of paired residues within the duplexes. (G) Classification of 3' UTR duplexes based on i) the absence of bulges (perfect duplex) or ii) the relative positioning and sizes of internal loops and bulges in the proximal and distal arms (symmetric, asymmetric with no bulges, or asymmetric with at least 1 bulge). Proportions of 3' UTR duplex types in STAU1 hiCLIP and PARIS data, respectively, grouped according to duplex span. (H) Summary of the STAU1 hiCLIP selectivity features (nucleotide composition and base-pairing architecture) compared to PARIS for example duplexes on the *SRSF1* 3' UTR (see also Supplementary Figure S5E). Distributions in (D–F) were compared with the Mann-Whitney test.

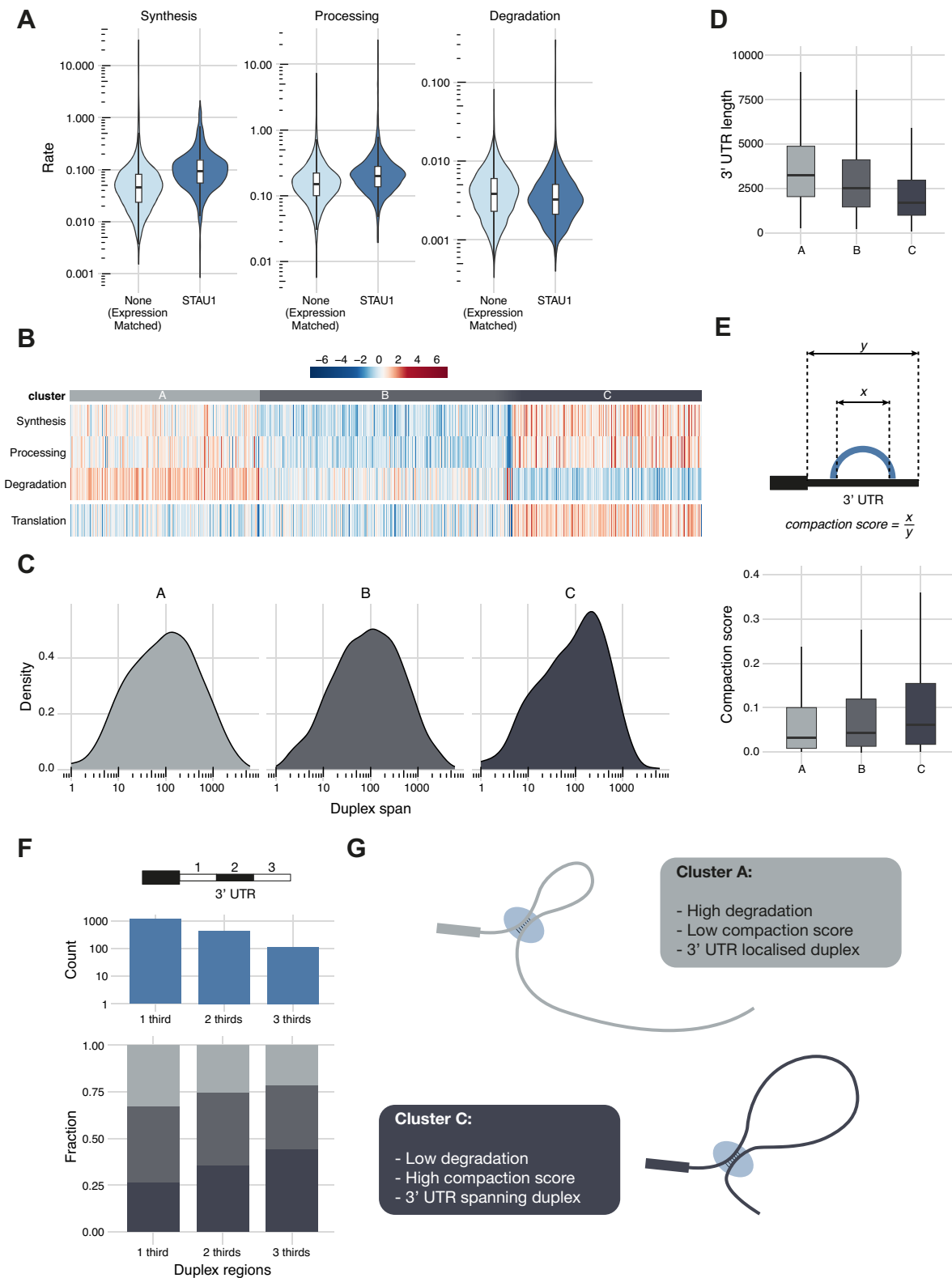


**Figure 6.** The relationship between STAU1 hiCLIP identified 3' UTR duplexes and RNA metabolism. (A) RNA metabolism (synthesis, processing and degradation rates) as measured by (5) for genes with 3' UTR duplexes identified by proximity ligation in STAU1 hiCLIP compared to genes without duplexes but matched for gene expression. (B) Above: RNA metabolism profiles clustered based on synthesis, processing and degradation rates estimated by (5) for genes with STAU1 hiCLIP identified 3' UTR duplexes. Below: Translation rates for these genes calculated by (5). (C) Mean 3' UTR duplex spans per gene for each cluster in (C). (D) 3' UTR lengths of the genes in each cluster. (E) Above: schematic describing the compaction score calculation. Below: compaction scores for the genes in each cluster. (F) Above: Number of genes with duplexes spanning one-, two- or three-thirds of the length of the 3' UTR. Below: Distribution of metabolism clusters for genes with duplexes spanning the three sub-segments of the 3' UTR. (G) Schematic model indicating the two types of 3' UTR duplex identified by STAU1 hiCLIP and their relationship with RNA degradation.



tected above. First we use pblat (19), using a step size of 5, tile size of 11 and minimum score of 15 (10) to identify all partial read alignments to the reference sequence. Next we filter the pblat output using a stringent e-value threshold of  $\leq 0.001$  to keep only high quality alignments. We also filter out reads with  $> 100$  partial alignments to keep the next step computationally tractable. Then we select all the best partial alignments for a given set of read start and end coordinates. If a read contains one partial alignment that spans the majority of the read, leaving only 15 nt unaligned, then it is deemed not to contain a hybrid and is filtered out. This prioritises non-hybrid solutions over hybrid solutions and helps control the false-positive detection of hybrids. If the read is not filtered out, then all the best partial alignments are cross-joined with each other to derive all possible combinations. These combinations then pass through three filters. First, any partial alignments that have  $> 4$  nt overlap or are more than 4 nt apart in the read sequence are removed. A small amount of leeway is allowed as feasibly a few nucleotides at the ends could be assigned to either hybrid arm. Second, any solutions where both partial alignments align to the same reference sequence, but that overlap regions of the reference sequence are removed. Third, those solutions that start  $> 5$  nt away from the crosslink position are removed. At this point, for reads that have a unique solution, this is selected as the hybrid alignment. For reads that have more than one solution, any solution that overlaps one of the unique solutions is selected as the hybrid alignment. If there is more than one overlap, then the solution with greatest total length of the read aligned is selected. Any reads that still have multiple potential solutions are deemed ambiguous and not analysed further as hybrid reads. PCR duplicates are then collapsed using the unique molecular identifiers with the directional method from UMI-tools (20) modified to consider the RNA transcript and start coordinates of both arms of the aligned hybrid.

*Delineation of duplexes using graph-based clustering of hybrids.* To delineate duplexes we developed a graph-based clustering approach to overcome limitations of the original coverage-based approach when dealing with larger datasets with greater complexity. We used BEDtools (14) to identify overlapping hybrids (requiring both hybrid arms to overlap) and then calculated the fraction of the overlap for each arm as a proportion of the total span of the two overlapping arms. Those with a fraction  $\geq 0.5$  for both arms were annotated as valid overlapping hybrids. Then we used these calculations to create an undirected graph using the igraph package (21) where nodes were hybrids and edges overlaps (weighted by the fraction overlap). From this graph, we identified the connected components (i.e. set of linked vertices) to derive subgraphs of hybrids that represented the same duplex that we termed clusters. To define the ends of a duplex from the clustered hybrids, we took the median start and end positions.

*Calculation of hybridisation energy.* To calculate the hybridisation energy for each duplex we used RNAduplex from the ViennaRNA package (22) to predict the minimum free energy duplex structure from the two arms, disallowing lonely pairs. We also calculated a control hybridisation

energy for each duplex as the mean minimum free energy from 100 iterations of shuffling the duplex arm sequences (preserving dinucleotide content) using uShuffle (23).

*Visualisation of hybrids.* Comprehensive hybrid data are stored as tables and can be used to visualise hybrids or duplexes as arc plots. Additionally, the relevant attributes from the hybrid tables are also used to generate BAM files to enable visualisation in genome browsers. Custom ‘ID’, ‘XP’, ‘CL’, ‘RO’ and ‘BE’ BAM tags are used to enable grouping or colouring by hybrid id, experiment or sample, duplex cluster, hybrid read orientation and hybridisation energy respectively in, for example, IGV (Integrative Genomics Viewer). Furthermore, duplexes are converted into BED files for visualisation. Optionally, selected genes of interest can be supplied and arc plots generated for viewing in IGV and nucleotide-resolution or binned contact map matrices for static plotting.

### Identification of RBP crosslink peaks from non-hybrid hiCLIP and iCLIP

To identify STAU1 crosslink peaks from hiCLIP reads in which no hybrids had been detected, and HuR and TDP-43 crosslink peaks from iCLIP data (E-MTAB-11854 and (24) respectively) we used the nf-core/clipseq (v. 1.0.0—Ianthine Pelican) pipeline with default parameters. Biological replicates for each RBP were processed separately to identify crosslinks and then merged using BEDTools (14) to create the input for the iCount peak caller. Significant crosslink sites were identified using a half-window setting of 10 nt for STAU1 and TDP-43 (on account of the broader binding profiles of these RBPs) and the default 3 nt for HuR. Peaks were calculated by merging significant crosslink sites within 10 nt (for STAU1 and TDP-43) and 3 nt (for HuR) of each other.

### Prediction of bound short-range duplexes from STAU1 non-hybrid reads

*Derivation of pairing probability profiles.* For all genes bound by STAU1, we defined a representative 3' UTR. This was selected by processing the matched HEK293 RNA-seq data from (2) using the nf-core/rnaseq pipeline (v3.1—Lead Alligator) with pseudoalignment using Salmon (25) to obtain transcripts per million values for each transcript. The 3' UTR from the most highly expressed transcript for each bound gene was selected. If transcripts for a bound gene were not detected in the RNA-seq (likely due to low abundance), we selected the longest annotated transcript isoform (with ties broken by a hierarchy of most exons followed by longest 3' UTR). For each 3' UTR sequence, we calculated the local pairing probability for each base using RNAplfold from ViennaRNA (22) using a window size of 100 nt. We also generated control pairing probabilities as the mean of the pairing probability from 100 iterations of shuffling the 3' UTR sequence (preserving dinucleotide content) using uShuffle (23).

We identified the probabilities in the  $-100$  to  $+100$  nt region centred on the STAU1 peak starts and for the metaprofiles calculated the mean and standard error of the mean.

We performed the same analysis for HuR and TDP-43. To cluster the STAU1 peaks based on the downstream structure profile, we extracted the probabilities in the +10 to +75 nt region and performed k-means clustering. We applied the silhouette method to guide the choice of number of clusters.

*Derivation of predicted STAU1-bound duplex structures.* To predict duplex structures downstream of STAU1 crosslink sites, we selected the peaks from the clusters with evidence of a downstream stem-loop structure. From the metaprofiles for each cluster we calculated the regions that contained the proximal and distal duplex arms relative to the peak start position. To identify the boundaries of these regions we calculated the local minima of the profiles, which described the arm ends. For each peak, we then extracted the sequences for these regions and used them as input to RNAduplex to identify the duplex contained within and trimmed unpaired flanking nucleotides.

### PARIS data processing

We trimmed sequencing adapters using Cutadapt and collapsed PCR duplicates in advance of alignment using the readCollapse.pl script used in the original publication (available at <https://github.com/qczhang/icSHAPE>). Subsequent processing was using Tosca as above.

### RIC-seq data processing

We trimmed sequencing adapters using Cutadapt and collapsed PCR duplicates prior to alignment using the remove\_duplicated\_reads.pl script used in the original publication (<https://github.com/caochch/RIC-seq>). Low-complexity fragments from each end of reads were then trimmed with Cutadapt as in the original publication. Paired reads were then merged with BBMerge. The merged FASTQ files were used as input for *Tosca* as above.

### Integration with RNA metabolism data

We used the processed data available from (5) quantifying RNA abundance (gene copy number) and RNA metabolism rates (synthesis, processing and degradation). To cluster the genes using the three rates, we log<sub>10</sub>-transformed the data and scaled and centred synthesis, processing and degradation rates to give them equal weighting in the clustering. We then used k-medoid clustering with 3 clusters, as identified using the silhouette method.

To corroborate the RNA degradation rates from (5) we compared them with transcript half-life measurements from (26), available as processed data, which were calculated using time-course RNA-seq after 4sU labelling, or after transcriptional shut-off with actinomycin D or  $\alpha$ -amanitin in duplicates. We calculated Spearman's rank correlation coefficients to test the correlation between each replicate and the degradation rates.

To identify relationships between STAU1-bound duplex span and 3' UTR length, we first identified a representative 3' UTR for a gene containing a duplex by selecting the longest 3' UTR from the gene that overlapped the duplex. To correct duplex span and 3' UTR length for intronic length (given that the STAU1 hiCLIP performed in

(2) is cytoplasmic and thus reflects mRNAs), we identified 3' UTR introns contained within either the duplex span or the 3' UTR and subtracted them respectively. We then calculated the compaction score as the duplex span divided by the 3' UTR length. This is analogous to the circularisation score defined previously (11), but substituting 3' UTR length for gene length.

## RESULTS AND DISCUSSION

### Hybrid reads contain intact and degraded linker sequences

We first reprocessed the publicly available STAU1 hiCLIP data (Sugimoto *et al.* 2015; Materials and Methods) by broadly replicating the original analysis. The dataset consists of two replicates (high and low RNase library preparation conditions) and contain 2 429 385 and 2 996 034 reads respectively. One of the original rationales for the linker adapter was to enable easy bioinformatic deconvolution of the two hybrid arms from a sequencing read (2). We identified the location of the full linker sequence in the read to extract 62 906 and 43 982 reads respectively, giving a total of 106 888 reads that contained hybrids (1). This compared with 72 280 and 46 502 in the original analysis, the difference owing to more stringent criteria (2).

First, we sought to recover hybrids containing degraded linker adapters (Figure 1A, purple). We therefore also examined the sequenced reads for truncated linker adapter sequences (with up to 2 nt lost from 3' end), and recovered a further 8324 and 5412 sequencing reads from the high and low RNase conditions respectively. Hence, although there is some degradation of the linker adapter, this is not a major source of lost hybrids.

Combining these two groups of linker hybrids, it was possible to reconstruct both arms after alignment for 21 285 and 12 884 hybrids in the high and low RNase conditions respectively. This compares with 21 291 and 14 067 in the original, where the more sensitive iterative mapping approach was able to be used. After UMI-aware collapsing of PCR duplicates, this left 11 429 and 4412 unique linker hybrids. Overall, this meant that 2 325 238 (95.7%) and 2 891 834 (96.5%) sequencing reads were classified as not containing linker adapters in the high and low RNase conditions respectively and formed the starting point for the subsequent analysis.

### Hybrid reads can form through direct proximity ligation in the absence of the linker adapter

Next, we explored the occurrence of hybrids from direct proximity ligation. This challenged the validity of the assumption that a linker adapter was necessary for proximity ligation. However, identifying the two arms of a hybrid within a sequencing read without the benefit of the linker to demarcate the join is challenging. Using a partial alignment and hybrid reconstruction approach on a read-by-read basis (implemented in the *Tosca* computational pipeline, Supplementary Figure S1, see Materials and Methods), we identified 92 422 and 58 186 such direct proximity ligation hybrid reads in the high and low RNase conditions respectively. Of these, 17 424 and 12 113 had more than one possible hybrid solution and so were filtered out as ambigu-

ous. After UMI-aware collapsing of PCR duplicates, this left 39 722 and 16 628 unique direct proximity hybrids. This was 3.6 times as many as were detected with a linker (Figure 2A). There were similar proportions for both low and high RNase conditions, suggesting that RNase digestion within this range does not preclude proximity ligation. As for hybrids with a linker, the majority of direct proximity ligated hybrids were intra-transcript (linker, 74.9% and direct, 77%, Figure 2B). Inter-transcript hybrids were predominantly between rRNA and mRNA, consistent with the known relationship between STAU1 and translation (2,27). There were also similar proportions of proximity ligation hybrids recovered from rRNA regions compared to hybrids with a linker (linker, 30.4% and direct, 34.2%, Figure 2C), and within mRNAs 3' UTR binding also dominated to a similar level (linker, 44.8% and direct, 42.5%, Figure 2C).

We then used the hybrid reads from each source to identify the duplexes they represented using a graph-based clustering approach. Using solely linker hybrids identified 734 mRNA duplexes. However, including the direct proximity ligation hybrids increased the yield 3.4-fold to 2515 (Figure 2D). Interestingly, only a minority—100—of all duplexes were found from both sources (Figure 2D). We found that genes with duplexes found in both datasets had a higher RNA abundance (Figure 2D, inset). Thus, the relatively low overlap likely reflects the sensitivity limits of this hiCLIP dataset. As we are sampling from the population of STAU1-bound duplexes, those on more abundant transcripts are more likely to be recovered by both approaches. Next, we focused on intra-transcript duplexes in mRNA and ncRNA: this showed that duplexes identified from direct proximity ligation reads had similar hybridisation energies (Figure 2E) and duplex spans, i.e. genomic distance between the two duplex arms (Figure 2F) to the ones identified from linker hybrids. So, the features of hybrids detected by linker and direct proximity ligation approaches are highly comparable, demonstrating that the direct proximity hybrids also originate from STAU1-bound duplexes. Thus, the linker and direct proximity ligation hybrids were combined for our subsequent analysis.

### ***In silico* read reconstruction shows not all hybrids are recoverable without a linker adapter**

Next, we wanted to assess the limitations of computational hybrid recovery of direct proximity ligation hybrids. The STAU1 hiCLIP dataset is uniquely placed for evaluating the performance of hybrid detection approaches because the linker unambiguously delineates each hybrid arm and their exact transcriptomic locations - thus, the linker hybrids constitute a 'ground truth' set of hybrids. To compare *Tosca* hybrid solutions to those identified by individual arm mapping, we took all the hybrid reads that contained a linker and removed the intervening linker adapter sequence. In this way we created 15 841 *in silico* direct proximity ligation hybrids, but for which we knew reliably both that they were hybrid reads and the transcripts and coordinates of the hybrid arms.

Processing these *in silico* hybrid reads using *Tosca* was very informative. Unique hybrid solutions were found for only 45.6% (7225) of the reads (Supplementary Fig-

ure S2A). Crucially, however, these solutions matched the known transcripts and coordinates in 97.2% of cases (Supplementary Figure S2A). The main differentiating factor appeared to be the length of the sequencing read, with unrecovered reads significantly shorter (Supplementary Figure S2B, median 58 v 68 nt,  $P < 2.2 \times 10^{-16}$ ). Furthermore, the length of the shorter arm fragment within a hybrid read was also significantly shorter (Supplementary Figure S2C, median 21 nt v 28 nt,  $P < 2.2 \times 10^{-16}$ ). It is likely that these shorter fragments align to multiple loci on the transcriptome and thus cannot be assigned uniquely; this prevents the reconstruction of a unique hybrid solution for these reads. There were no differences between high or low RNase digestion conditions (Supplementary Figure S2B, C). Generally, a much smaller proportion of inter-transcript hybrids could be recovered (Supplementary Figure S2D), however there were unrecovered hybrid arms across all RNA types and regions (Supplementary Figure S2E).

Importantly, this analysis using real (rather than synthetic) data shows that our computational approach can recover direct proximity ligation hybrids with high accuracy. It also demonstrates the importance of an adequately long cDNA to be able to do so. There is a balance between the level of RNase digestion, sequencing read length and maintaining the spatial resolution of the identified structure: we would recommend reads at least 75, if not 100 nt long and that RNase digestion is titrated so that each hybrid arm is at least 25–30 nt long.

### **Non-hybrid reads help derive STAU1-bound short-range duplexes**

While the new methods described thus far have considerably improved the recovery of hybrids from the STAU1 hiCLIP data, for 2 383 462 and 2 946 736 of the reads in the high and low RNase conditions we were ultimately unable to resolve a hybrid after mapping and hybrid identification and were thus non-hybrid reads. Owing to the stringent purification steps, these non-hybrid reads still represent sites where STAU1 has crosslinked to specific transcripts and thus reflect STAU1 binding. We set out to explore whether they could additionally represent short duplex structures whose loop regions were protected from RNase digestion (Figure 1A, turquoise panel). We anticipated that such duplexes would have short loops and so to search for them, we developed a computational workflow to derive stem-loops near STAU1 crosslink peaks. We focused on 3' UTRs because the majority of STAU1 crosslinking peaks (7.4%) are located in this region (Figure 3A), but this approach is extendible to other transcript regions.

To explore the secondary structure around 3' UTR STAU1 crosslink peaks, we first calculated the local base-pairing probability of each nucleotide and generated a meta-profile centred on the peak start position (Figure 3B). As expected, there is a sharp trough in base-pairing probability around position 0, consistent with UV-crosslinking generally being much more efficient at unpaired nucleotides (28). Strikingly, there is an 'M'-shaped profile in the +10 to +75 nt region (shaded grey), that reflects a tendency for a paired-unpaired-paired secondary structure motif downstream of the peak start, viz. a stem loop structure, with



the paired regions the two arms of the stem, and a short intervening unpaired loop. This pattern is absent in control shuffled 3' UTR sequences (dashed red line). Furthermore, this structural motif is absent around crosslink peaks of other known 3' UTR binding single stranded RBPs, such as HuR and TDP-43 (Figure 3B). Crosslinking between RBP and RNA primarily occurs at unpaired nucleotides, so STAU1 crosslinks are expected in three locations: upstream of a paired region, in the loop itself or downstream of a paired region. However, in practice, the experimental method and library preparation will advantage reads that contain at least part of the paired region as they are protected from the single-stranded RNase leaving longer RNA fragments (2). Furthermore, crosslinking is less likely to occur in the hairpin loops, given our prediction that they are likely to be short. Thus, STAU1 crosslinking upstream of a paired region is likely to dominate, as we observe here with the predicted 'M' structural motif.

Next, we focused on the individual peaks to characterise the presence of this structural motif further (Figure 3C). We used k-means clustering to group peaks based on the pairing probability profiles in the +10 to +75 nt region. Applying the silhouette method identified two major clusters of non-hybrid peaks: those containing the 'M'-shaped profile (7339, 66.6%) and those that did not (3678, Figure 3C, Cluster 0; Supplementary Figure S3A). Thus cluster 0 represents those peaks without a downstream stem-loop structure and were not considered further. The peaks with a 'M'-shaped profile were further grouped into three separate sub-clusters (Figure 3C, Clusters 1–3), each differing in the distance from the STAU1 crosslink peak start (Cluster 1 closest starting at 1 nt, followed by Cluster 2 at 8 nt and Cluster 3 furthest away at 16 nt).

Finally, we predicted the RNA secondary structures to which these pairing probabilities correspond. For each cluster we defined the regions that are most likely to form duplexes by calculating the local minima of the pairing probability metaprofile (Supplementary Figure S3B). This identified the duplex-containing regions as positions 1–25 (proximal arm) and 26–46 (distal arm) for Cluster 1; 8–31 and 32–54 for Cluster 2; and 16–38 and 39–63 for Cluster 3. Then we derived the corresponding RNA secondary structures by computationally hybridising the proximal and distal arm sequences (Figure 3D). The majority of derived duplexes (87.7%) were 8 bp or longer with hybridisation energies indicating they were more stable than their shuffled controls (Figure 3E,  $P < 2.2 \times 10^{-16}$ ). NMR studies have found that stems of at least 8 bp were needed for STAU1 to bind (29), thus we excluded the small fraction (8%) of predicted duplexes that were shorter than 8 bp from the subsequent analysis as they likely did not represent robustly bound structures (Figure 3E). Thus, we obtained a final set of 6366 duplexes that we term 'derived' duplexes.

Our hypothesis was that these structures avoided digestion by RNase treatment owing to their short loops and steric protection by the bound STAU1 protein. Hence we assessed the loop lengths of our derived structures (Figure 3F). The median loop length was indeed short at 7 nt with 75% of the loops <10 nt. Furthermore, we would expect these structures to be largely absent from the atlas of duplexes derived from hybrid reads.

We pooled all the experimentally-detected proximity ligation hybrids (linker and direct) and the derived duplexes, and applied our graph-based clustering approach to consolidate them into a complete atlas of STAU1-bound duplexes (Figure 3G). We assessed how many duplexes were supported by one or more sources: 4198 were detected by proximity ligation, of which 1281 were supported by both direct ligation and linker hybrids. As expected, only a small fraction of the atlas (1.4%; 143) of duplexes overlapped derived structures (Figure 3G). Altogether, using the graph-based clustering (rather than the less stringent original coverage-based approach) to identify experimentally-supported duplexes and incorporating the predicted duplexes, we recovered 10 522 STAU1-bound duplexes (excluding rRNA) (Figure 3G), a ~10-fold increase from the original.

### ***Tosca*: a nextflow pipeline for proximity ligation data analysis and visualisation**

We developed a Nextflow computational pipeline, *Tosca*, to enable robust, reproducible and scalable implementation of our analysis approach (<https://github.com/amchakra/tosca>). Reference transcriptomes are provided for human, mouse and rat, but custom references can also be user-provided. *Tosca* performs transcriptomic alignment and hybrid read identification and PCR de-duplication. This is followed by conversion to genomic coordinates and hybrid annotation. Graph-based clustering of hybrids enables delineation of the duplexes they represent. For these, hybridisation energies are calculated to assess duplex stability (Supplementary Figure S1).

Importantly, *Tosca* also focuses on data visualisation and exploration. It generates BAM files that can be loaded in IGV as tracks to interactively display hybrids in the genome browser (Supplementary Figure S4) with additional meta-data enabling grouping and/or colouring by experiment or sample, duplex cluster, hybrid read orientation or hybridisation energy. Additionally, arc files for IGV can be generated for user-specified genes. Furthermore, files are generated to enable easy static plotting as arc plots (Figure 4A) or as contact map matrices (Figure 4B).

The *Tosca* pipeline can be run from the command-line using a single command to Nextflow that specifies the input files, transcriptome and additional customisable parameters. All the dependencies are containerised using Docker to ensure hassle-free deployment across platforms. We have provided user documentation in the repository and *Tosca* remains under active development.

### **Comparison with global duplexes reveals insights into the RNA selectivity of STAU1**

Our computationally-enhanced atlas finally enabled us to proceed with contextualising the STAU1-bound structures in the landscape of RNA structures globally. We used publicly available psoralen-based proximity ligation data in HEK293 cells generated using PARIS as a description of global RNA structures: both bound and not-bound by RBPs (4). Additionally, we analysed publicly available RIC-seq data (albeit from HeLa cells), as a description of globally-captured RNA-RNA interactions mediated by RBPs, both associated or not with base-pairing (30).

Briefly, hiCLIP, PARIS and RIC-seq share conceptual and methodological key steps, but it is necessary to understand the technical details pertaining to each that enrich different types of RNA interactions to interpret these comparisons. The two most important steps in which the methods differ are: (i) the stabilisation of RNA-RNA interactions and (ii) their purification. Both STAU1 hiCLIP and PARIS enrich for interactions mediated by base-pairing, by virtue of UV crosslinking and purification of STAU1, which specifically binds dsRNA (hiCLIP) and psoralen crosslinking dsRNA (PARIS). In contrast, RIC-seq employs formaldehyde (FA) crosslinking to stabilise interactions. FA crosslinks protein-RNA and protein-protein interactions, thus interactions obtained by RIC-seq include not only RBP-mediated duplexes, but also RNA-RNA contacts mediated by an RBP or protein-protein interactions, which may not involve base-pairing interactions or extended/stable duplexes. Therefore, PARIS and RIC-seq provide two different reference global datasets to compare our STAU1 data against: PARIS as representative of duplexes, and RIC-seq as representative of protein-mediated interactions.

To ensure a valid comparison, we re-processed the PARIS and the RIC-seq data using *Tosca* with the same gene annotations as for the hiCLIP analysis, and clustered the hybrid reads to generate an atlas of 116 929 intra-transcript duplexes for PARIS (excluding rRNA and tRNA) from 537 448 unique hybrids across three biological replicates) and 63 966 unique intra-transcript interactions for RIC-seq (excluding rRNA and tRNA, from 944 663 unique hybrids across two biological replicates).

Duplexes recovered experimentally (i.e. through proximity ligation) likely reflected a separate group of STAU1-bound structures compared to those recovered through computational derivation (for which only 3' UTR regions were considered) (Figure 5A, B). We kept them separate for the subsequent comparative analyses to explore this further, and to avoid introducing bias to comparisons with PARIS or RIC-seq. The regional distribution (excluding intronic regions) of duplexes for PARIS was similar to that originally obtained, with the majority in the CDS, followed by the 3' UTR. The RIC-seq distribution of interactions over selected regions was similar to PARIS, consistent with the two methods sampling global RNA-RNA interactions. This compared with the vast majority of STAU1-bound duplexes (86.7%) linking 3' UTR regions (Figure 5A). Given the strong selectivity of STAU1 for 3' UTRs, we focused all subsequent comparisons on 3' UTR intra-transcript duplexes: 2872 were experimentally identified by STAU1 hiCLIP, 19 787 by PARIS, and 8810 by RIC-seq. There was only a small overlap between the hiCLIP and global sets of duplexes (1.9% were common to hiCLIP and PARIS datasets and 4.1% common to hiCLIP and RIC-seq datasets) (Supplementary Figure S5A). This is consistent with previous findings for PARIS and likely reflects the low sensitivity of RNA proximity-ligation methods in capturing the entirety of RNA structures.

As previously noted, STAU1 often binds long-range 3' UTRs duplexes, which can span intervening regions over 100 nt in length, and in some cases even kilobases (2). The proximity ligation atlas maintained the bimodal dis-

tribution of 3' UTR duplex spanning loop lengths for STAU1 observed earlier (Figures 2F and 5B). Fitting a two-component Gaussian mixture model revealed a primary peak ( $\lambda = 0.53$ ) with a mean duplex span of 252 nt and a secondary peak ( $\lambda = 0.46$ ) with a mean duplex span of 18 nt (Supplementary Figure S5B). For global RNA duplexes from PARIS, however, there was a unimodal distribution with a median duplex span of 63 nt (Figure 5B). The RIC-seq median span is 113 nt, suggesting that 3' UTR looping mediated by RBPs tends to span wider regions than 3' UTR structures generally. Overall, this reinforces the finding that STAU1 preferentially binds long-range 3' UTR duplexes, rather than this being a general feature of 3' UTR duplexes.

We next sought to describe the stability and the features of 3' UTR intra-transcript contacts for STAU1 hiCLIP compared to the other methods. Because some of the metrics we calculate for our comparisons are dependent on interaction length, which in turn is dependent on the original hybrid arm length, we first assessed the latter for STAU1 hiCLIP, PARIS and RIC-seq datasets (Supplementary Figure S5C). While STAU1 and hiCLIP arms were of similar length (hiCLIP median 33 nt vs PARIS median 28 nt), RIC-seq arm lengths were much longer, with a median of 62 nt. This marked difference in read length was mirrored in the length of the interactions after clustering the hybrid reads. Thus for the subsequent comparisons between hiCLIP and RIC-seq data, we only evaluated the length-corrected metrics.

Given the non-uniform distribution of duplex spans for STAU1-bound duplexes, we classified them into short-range (<25 nt, 817 duplexes), medium-range (25–100 nt, 723 duplexes), long-range (>100 nt, 1332 duplexes) and derived (6206 duplexes).

We found that despite similar ranges of arm lengths, STAU1 hiCLIP duplexes had more bases paired compared to PARIS (median 20 nt versus median 15 nt,  $P = < 2.2 \times 10^{-16}$ , Figure 5C). RIC-seq had a markedly higher number of paired residues than either PARIS or hiCLIP, but we attribute this to the more extended interacting arms (Figure 5C, Supplementary Figure S5C).

To assess stability, given the differences in number of paired residues for each experiment, we normalised the hybridisation energy of the interactions by the total number of paired residues. We found that while both STAU1 and PARIS duplexes and RIC-seq interactions were more thermodynamically stable than their shuffled controls ( $P < 2.2 \times 10^{-16}$ , and  $P < 2.2 \times 10^{-16}$ , Figure 5D), STAU1 proximity ligation duplexes were also on average more stable than PARIS duplexes ( $P = 6.19 \times 10^{-178}$ ) or RIC-seq interactions ( $P = 2.51 \times 10^{-60}$ ) (Figure 5D). While this could reflect a predilection of STAU1 to bind more stable structures, it is more likely to result from technical differences in the hiCLIP and other experimental protocols. In hiCLIP, UV crosslinking of the RBP to the RNA is the only stabilising factor during the mild washing of beads performed before the proximity ligation, and so it is probable that less stable structures are lost through the lysis and washing steps. However, in PARIS psoralen directly crosslinks the RNA duplexes so they are more likely to be preserved through the experimental steps. In RIC-seq, the interactions are sta-



bilised with FA and proximity ligation is performed *in situ*, so interactions are maintained and captured despite thermodynamic lability. Additionally, for RIC-seq interactions that are mediated by RBPs, the RNAs can be brought in proximity by the protein itself, without the requirement for a strong base-pairing potential. Moreover, derived STAU1-bound duplexes have a similar hybridisation energy profile to PARIS duplexes, consistent with their representing weaker or transient interactions that are lost through the stringent hiCLIP washes.

Intriguingly, we noted that the hybridisation energies for the shuffled controls, where dinucleotide content had been preserved, were more negative for PARIS and RIC-seq than for STAU1 hiCLIP. This led us to question whether there were differences in GC content; STAU1 hiCLIP duplexes were indeed significantly more AU-rich when compared with PARIS duplexes or RIC-seq interactions (Figure 5E) and furthermore this was most dramatically the case for the long-range duplexes (median 45.4% versus PARIS median 33.3%,  $P = 1.25 \times 10^{-119}$ , versus RIC-seq median 29.6%,  $P = 6.41 \times 10^{-149}$ ).

Examining the duplex structures in more detail, we observed that more of the residues in the STAU1 duplexes were involved in base-pairing than in the PARIS duplexes and RIC-seq interactions (Figure 5F, STAU1 median 83% vs PARIS median 77%,  $P = 4.2 \times 10^{-238}$ , vs RIC-seq median 68%,  $P < 2.2 \times 10^{-16}$ ). This prompted us to explore the composition of the duplexes in terms of bulges (i.e. single-nucleotide unpaired residues within the stem) and internal loops. Because the following measurements are directly linked to hybrid lengths, which are only comparable for PARIS and hiCLIP, and because RIC-seq data also contains interactions that are not driven by duplex formation (as discussed above), we only compared the STAU1 and PARIS structural features. We found that while there were similar numbers of bulges or internal loops overall in the two (Supplementary Figure S5D, median 3 vs 3 for proximity ligation duplexes and 2 for predicted duplexes), their positioning differed: symmetry was an important distinguishing feature. While both sets had a small fraction of perfect duplexes and consisted mostly of asymmetric duplexes, for STAU1 hiCLIP, there was a higher proportion of symmetrical duplexes (i.e. with identically-sized bulges or internal loops in both arms at the same position within the stem), 12.7–19.4% (mean: 16.2%) vs 6.1–6.8% (mean: 6.5%), despite these duplexes being longer (Figure 5G). Among asymmetric duplexes, for both STAU1 and PARIS, a large fraction contained at least one bulge, which is a destabilising element. However, the long range STAU1 interactions have a slightly lower fraction compared with short and medium range interactions, suggesting that a fraction of long-spanning duplexes bound by STAU1 owe their stability in part to the absence of bulges. Interestingly, STAU1-bound derived duplexes share symmetry characteristics with proximity ligation duplexes (Figure 5G), supporting that they are specific for STAU1, but thermodynamic features with PARIS duplexes (Figure 5D), likely reflecting that they capture weaker or more transient interactions lost during the hiCLIP experimental steps.

Given the observed selectivity for symmetry in STAU1 hiCLIP and the preponderance of asymmetric duplexes, we characterised them in more detail. Even among these, STAU1 hiCLIP proximity ligation duplexes displayed a higher degree of symmetry, indicated by a higher percentage of all bulges or internal loops having a symmetrically positioned identical element in the other arm (Supplementary Figure S5E). In contrast, many asymmetric PARIS duplexes did not have a single position with such symmetry. Additionally, asymmetric STAU1 proximity ligation duplexes tend to have longer bulge or internal loop-free stem segments (i.e. larger stretches with contiguous pairing) compared to PARIS (Supplementary Figure S5F).

Although our observed STAU1 features preferences may in part be attributable to technical differences between hiCLIP and PARIS (e.g. duplex stabilisation and purification methods), our findings are consistent with other biochemical and modelling studies. Intriguingly, the original NMR studies exploring the mechanisms of Staufen double-stranded RNA binding domain recognition of dsRNA found, through generation of synthetic stem loops that disruption of the helical structure through the introduction of bulges significantly reduced binding (29). Furthermore, our results are consistent with a previous computational model of *Drosophila* Staufen binding that found a preference for stems in which at least one side spans 12 nt and with few unpaired bases or internal loops (31). The preservation of structural symmetry may reflect the importance to STAU1 binding of a particular kind of tertiary conformation.

In summary, the principal features of STAU1-bound duplexes remain consistent across the span of duplexes, with an increase in A:U base pairs, symmetry and lack of bulges for the long-range interactions spanning more than 100 nt. By comparing STAU1 hiCLIP detected duplexes with global 3' UTR RNA duplexes determined using PARIS, we have been able to assess characteristics of the proximity ligation duplexes that are enriched in the former, such as 3' UTR binding, long-range loops, and symmetrical stems with more bases paired, all suggestive of the nature of STAU1 binding to RNA structures (Figure 5H). The key features distinguishing the duplexes recovered by the two proximity ligation methods are highlighted in two illustrative examples on the *SRSF1* 3' UTR (Figure 5H, Supplementary Figure S5G). Evidence to-date suggests that STAU1 likely recognises a predominantly structural, rather than sequence, motif through interactions with the dsRNA backbone (31,32). Our findings support this hypothesis. However, while the GC-rich long base-paired regions of the well-studied *ARF1* binding site are thought to contribute to duplex stability, our data suggest a more complex picture related to the span of the given duplex. Notably, long-range duplexes are AU-rich, and therefore thermodynamically less favourable. However, they have longer, more symmetrical stems, with more base pairing (Figure 5H) that is not evident in the global duplexes detected by PARIS. This requirement for specific lengths and structural conformations, rather than thermodynamic stability, to enable regulatory function is reminiscent of one recently described in the context of ribosome stalling (33).

### Integration with RNA metabolism reveals a putative role of selected 3' UTR RNA duplexes

STAU1 is known to be involved in RNA metabolism, most notably RNA degradation (7,8), but also translation (34). To explore the role of RNA structure in this regulation, specifically STAU1 hiCLIP-identified duplexes, we integrated our expanded atlas with publicly available functional RNA data also in HEK293 cells that used metabolic labelling (4sU-seq) and mathematical modelling to measure synthesis, processing and degradation rates of RNAs (5). Given the predominance of STAU1 3' UTR binding we again focused on this region.

First, we categorised genes into three groups on the basis of sources of their detected 3' UTR duplexes: (i) containing STAU1 hiCLIP (and/or PARIS) duplexes (STAU1 genes), (ii) containing only PARIS duplexes (PARIS genes) or (iii) not containing any detected duplexes. We then used the gene copy numbers calculated using spike-ins by (5) to assess for differences in RNA abundance (Supplementary Figure S6A). We noted that genes in which no 3' UTR duplexes were detected had a significantly lower expression level than those identified by PARIS or STAU1 hiCLIP. This marked difference likely reflects the sensitivity and detection limits of the methods. Consequently, for the subsequent comparative analysis we curated a set of 5633 genes with an expression level greater than the 5th percentile of genes with PARIS or STAU1 hiCLIP duplexes. We did not include the RIC-seq data in this metabolism analysis owing to the different cell type.

We used the calculated RNA metabolism rates to assess the different levels of synthesis, processing and degradation for these two categories of genes with identified 3' UTR duplexes (Figure 6A). This showed STAU1 hiCLIP genes to have significantly higher synthesis and processing rates than genes without duplexes (Mann-Whitney test,  $P < 2.2 \times 10^{-16}$  and  $P < 2.2 \times 10^{-16}$  respectively) and significantly lower degradation rates (Mann-Whitney test,  $P < 1.13 \times 10^{-12}$ ). Given the known role of STAU1 in RNA degradation through Staufen-mediated decay (7) this was a surprising finding. However, Staufen-mediated decay may only apply to a subset of transcripts. There was also a similar pattern when compared to genes with PARIS 3' UTR duplexes, notably so for degradation rates (Supplementary Figure S6B). At a transcriptome-wide level, genes with STAU1-bound 3' UTR duplexes have a lower degradation rate than genes with 3' UTR duplexes without STAU1 binding. This prompted us to explore this relationship further.

Examining the distributions of RNA metabolism rates of the STAU1 hiCLIP genes revealed heterogeneity in their profiles (Figure 6B). By using k-medoids clustering we could resolve the genes into three distinct clusters: (A) with intermediate synthesis and processing rates and high degradation rates (522 genes); (B) with low synthesis and processing rates and intermediate degradation rates (694 genes) and (C) with high synthesis and processing rates and low degradation rates (519 genes).

Given our interest in RNA degradation, we sought to corroborate these findings and identified three additional datasets in HEK293 cells that used 4sU labelling, actino-

mycin D treatment or  $\alpha$ -amanitin treatments to measure degradation transcriptome-wide (26). Reassuringly, there was good correlation between these measured half-lives and the calculated RNA degradation rates generally (Supplementary Figure 6C) and comparing them for the three clusters supported our initial groupings (Supplementary Figure 6D).

We next assessed the RNA translation of the transcripts in these different clusters using the translation potential measurements calculated from ribosome profiling data also in HEK293 cells (5,35). Strikingly this separates cluster C from the other two: those transcripts with a low degradation rate (and high synthesis and processing rates) are associated with a higher translation potential. This anti-correlation between RNA degradation and RNA translation makes biological sense; the longer a transcript is present in the cell, the longer it is available for the ribosome to translate; and this is consistent with the literature (36).

Interestingly, cluster C - with the low degradation rate - also had a shift in the distribution of 3' UTR duplexes span towards long-range duplexes (Figure 6C). This was not reflected in the overall 3' UTR length, where there was a significant shortening in 3' UTR length with reducing degradation rates (Figure 6D, Kruskal-Wallis test,  $P < 2.2 \times 10^{-16}$ ) as expected given the known relationship between 3' UTRs and RNA stability (37–39).

It appears that these long-range 3' UTR duplexes identified by STAU1 hiCLIP compensate for the degradation effect of longer 3' UTRs. To quantify this we adapted the concept of circularisation score (11) to the 3' UTR. We calculated a compaction score as the ratio of the STAU1 duplex span to the corresponding 3' UTR length: a higher score indicates more compaction of the 3' UTR by the STAU1 duplexes (Figure 6E). This showed that cluster C had a significantly higher compaction score than either A or B (Figure 6E, Dunn's test, adjusted  $P = 7.90 \times 10^{-8}$  and  $P = 7.55 \times 10^{-4}$  respectively).

To explore this effect in an alternative way, we assessed the positions of the proximal and distal duplex arms on the 3' UTR (Figure 6F). We divided 3' UTRs into thirds and calculated which thirds were spanned by the two arms. This showed that duplexes generally tended to be located towards the start of 3' UTR. Furthermore, longer-range duplexes spanning more thirds were proportionally greater in cluster C, again supporting a relationship between duplex span and degradation rates. Altogether, this suggests that there are two ends to the functional spectrum of genes with STAU1 hiCLIP identified duplexes (Figure 6G). One (represented by cluster A) has short range structures, often at the proximal end of the 3' UTR, reflected in a low compaction score and with a high degradation rate; the other (represented by cluster C) has long-range duplexes that can span the whole 3' UTR, compacting it, reflected in a high compaction score, and with a lower degradation rate. Thus, we can link these RNA structures to RNA degradation, and suggest a potential protective effect of these long-range duplexes on degradation.

The integrative computational analysis we present here examines the RNA metabolism features of genes with STAU1 hiCLIP identified 3' UTR duplexes and identifies a correlative relationship between the two. The original

RNA-seq data identified a very subtle overall abundance change for mRNAs containing 3'UTR hiCLIP duplexes when comparing STAU1 knockdown and rescue conditions (2), but this is unlikely to be related to the much more dramatic changes in mRNA stability observed between the mRNA groups identified in our study. Moreover, steady state assessments of transcript abundance cannot be directly compared with methods that measure transcript dynamics. Thus we anticipate that our findings provide a basis for a future mechanistic assessment of the roles played by the 3' UTR RNA structures, which may not necessarily relate to the roles of Staufen proteins.

In conclusion, first, we have extended the atlas of STAU1-bound duplexes ~10-fold primarily through: demonstrating that i) direct proximity ligation occurs at sufficient levels in the absence of a linker adapter; and ii) short-range STAU1-bound duplexes exist, but cannot be recovered through proximity ligation and require computational derivation. Thus we propose that the linker adapter can be omitted from the hiCLIP protocol. Second, we have developed a robust, reproducible and scalable computational pipeline, *Tosca*, which is broadly applicable to multiple kinds of proximity ligation methods and includes downstream duplex characterisation and visualisation. Finally, we have integrated our atlas (i) with global RNA duplexes to determine features of STAU1 RNA selectivity and (ii) with RNA metabolism rates to uncover putative relationships between RNA structure and degradation.

## DATA AVAILABILITY

All analysis code and RMarkdown notebooks to regenerate the figures are available at <https://github.com/luslab/comp-hiclip>. *Tosca* is available at <https://github.com/amchakra/tosca>. The pipeline is also deposited on Zenodo: <https://doi.org/10.5281/zenodo.7728671>. Publicly available data was used for this project. Raw STAU1 hiCLIP data is available from ArrayExpress at E-MTAB-2937 with matched RNA-seq data at E-MTAB-2940. Raw PARIS data is available from GEO at GSE74353. Raw RIC-seq data is available at GEO under accession number GSE127188. Raw RNA metabolism data is available from GEO at GSE84722, with processed data obtained from the supplementary files. Raw RNA degradation data is available from GEO at GSE99517, with processed data obtained from the supplementary material. HuR and TDP-43 iCLIP data are available from ArrayExpress at E-MTAB-11854 and E-MTAB-4733 respectively.

## SUPPLEMENTARY DATA

[Supplementary Data](#) are available at NAR Online.

## ACKNOWLEDGEMENTS

We would like to thank Dr Neelanjan Mukherjee for sharing normalisation code for the RNA metabolism data. We would also like to thank the members of the Luscombe and Ule labs for fruitful discussions, in particular Dr Yoichiro Sugimoto, Dr Federico Agostini, Dr Charlotte Capitanchik and Dr Chris Cheshire. For the purpose of Open Access, the

author has applied a CC BY public copyright licence to any Author Accepted Manuscript version arising from this submission.

*Author Contributions:* AMC: Conceptualisation, Methodology, Software, Formal Analysis, Investigation, Writing - Original Draft, Visualisation. IAI: Software, Formal Analysis, Investigation, Writing - Original Draft, Visualisation. FCYL: Investigation, Writing - Review & Editing. JU: Conceptualization, Writing - Review & Editing, Supervision. NML: Conceptualization, Writing - Review & Editing, Supervision.

## FUNDING

Wellcome Trust [FC010110; 215593/Z/19/Z]; Francis Crick Institute which receives its core funding from Cancer Research UK [FC010110]; UK Medical Research Council [FC010110]; Wellcome Trust [FC010110]; A.M.C. was supported by a Wellcome Trust PhD Training Fellowship for Clinicians Award [110292/Z/15/Z]; Crick Postdoctoral Clinical Fellowship and Academy of Medical Sciences Starter Grant for Clinical Lecturers [SGL023\1085]; F.C.Y.L. was supported by a Wellcome Trust Four-Year PhD Studentship [105202/Z/14/Z]; Wellcome Trust Joint Investigator Awards [215593/Z/19/Z to J.U. and N.M.L.]; N.M.L. is a Winton Group Leader in recognition of the Winton Charitable Foundation's support towards the establishment of the Francis Crick Institute; N.M.L. is additionally supported by core funding from the Okinawa Institute of Science & Technology Graduate University. Funding for open access charge: Wellcome Trust.

*Conflict of interest statement.* None declared.

## REFERENCES

- Sugimoto, Y., Chakrabarti, A.M., Luscombe, N.M. and Ule, J. (2017) Using hiCLIP to identify RNA duplexes that interact with a specific RNA-binding protein. *Nat. Protoc.*, **12**, 611–637.
- Sugimoto, Y., Vigilante, A., Darbo, E., Zirra, A., Militti, C., D'Ambrogio, A., Luscombe, N.M. and Ule, J. (2015) hiCLIP reveals the in vivo atlas of mRNA secondary structures recognized by Staufen 1. *Nature*, **519**, 491–494.
- Helwak, A., Kudla, G., Dudnakova, T. and Tollervey, D. (2013) Mapping the human miRNA interactome by CLASH reveals frequent noncanonical binding. *Cell*, **153**, 654–665.
- Lu, Z., Zhang, Q.C., Lee, B., Flynn, R.A., Smith, M.A., Robinson, J.T., Davidovich, C., Gooding, A.R., Goodrich, K.J., Mattick, J.S. *et al.* (2016) RNA duplex map in living cells reveals higher-order transcriptome structure. *Cell*, **165**, 1267–1279.
- Mukherjee, N., Calviello, L., Hirsekorn, A., de Pretis, S., Pelizzola, M. and Ohler, U. (2017) Integrative classification of human coding and noncoding genes through RNA metabolism profiles. *Nat. Struct. Mol. Biol.*, **24**, 86–96.
- Zheng, D., Cho, H., Wang, W., Rambout, X., Tian, B. and Maquat, L.E. (2020) 3'READS + RIP defines differential Staufen1 binding to alternative 3'UTR isoforms and reveals structures and sequence motifs influencing binding and polysome association. *RNA*, **26**, 1621–1636.
- Kim, Y.K., Furic, L., Desgrois, L. and Maquat, L.E. (2005) Mammalian Staufen1 recruits Upf1 to specific mRNA 3'UTRs so as to elicit mRNA decay. *Cell*, **120**, 195–208.
- Park, E. and Maquat, L.E. (2013) Staufen-mediated mRNA decay. *Wiley Interdiscip. Rev. RNA*, **4**, 423–435.
- Kaufmann, G., Klein, T. and Littauer, U.Z. (1974) T4 RNA ligase: substrate chain length requirements. *FEBS Lett.*, **46**, 271–275.
- Travis, A.J., Moody, J., Helwak, A., Tollervey, D. and Kudla, G. (2014) Hyb: a bioinformatics pipeline for the analysis of CLASH



- (crosslinking, ligation and sequencing of hybrids) data. *Methods*, **65**, 263–273.
11. Aw, J.G.A., Shen, Y., Wilm, A., Sun, M., Lim, X.N., Boon, K.-L., Tapsin, S., Chan, Y.-S., Tan, C.-P., Sim, A.Y.L. *et al.* (2016) In vivo mapping of eukaryotic RNA interactomes reveals principles of higher-order organization and regulation. *Mol. Cell*, **62**, 603–617.
  12. Sharma, E., Sterne-Weiler, T., O'Hanlon, D. and Blencowe, B.J. (2016) Global mapping of human RNA-RNA interactions. *Mol. Cell*, **62**, 618–626.
  13. Chan, P.P. and Lowe, T.M. (2016) GtRNAdb 2.0: an expanded database of transfer RNA genes identified in complete and draft genomes. *Nucleic Acids Res.*, **44**, D184–D19.
  14. Quinlan, A.R. (2014) BEDTools: the Swiss-Army tool for genome feature analysis. *Curr. Protoc. Bioinformatics*, **47**, 11.12.1–11.12.34.
  15. König, J., Zarnack, K., Rot, G., Curk, T., Kayikci, M., Zupan, B., Turner, D.J., Luscombe, N.M. and Ule, J. (2010) iCLIP reveals the function of hnRNP particles in splicing at individual nucleotide resolution. *Nat. Struct. Mol. Biol.*, **17**, 909–915.
  16. Martin, M. (2011) Cutadapt removes adapter sequences from high-throughput sequencing reads. *EMBnet journal*, **17**, 10–12.
  17. Dobin, A., Davis, C.A., Schlesinger, F., Drenkow, J., Zaleski, C., Jha, S., Batut, P., Chaisson, M. and Gingeras, T.R. (2013) STAR: ultrafast universal RNA-seq aligner. *Bioinformatics*, **29**, 15–21.
  18. Di Tommaso, P., Chatzou, M., Floden, E.W., Barja, P.P., Palumbo, E. and Notredame, C. (2017) Nextflow enables reproducible computational workflows. *Nat. Biotechnol.*, **35**, 316–319.
  19. Wang, M. and Kong, L. (2019) pblat: a multithread blat algorithm speeding up aligning sequences to genomes. *BMC Bioinformatics*, **20**, 28.
  20. Smith, T., Heger, A. and Sudbery, I. (2017) UMI-tools: modeling sequencing errors in Unique Molecular Identifiers to improve quantification accuracy. *Genome Res.*, **27**, 491–499.
  21. Csardi, G. and Nepusz, T. (2006) The igraph software package for complex network research. *InterJournal*, **1695**, 1–9.
  22. Lorenz, R., Bernhart, S.H., Höner zu Siederdisen, C., Tafer, H., Flamm, C., Stadler, P.F. and Hofacker, I.L. (2011) ViennaRNA Package 2.0. *Algorithms Mol. Biol.*, **6**, 26.
  23. Jiang, M., Anderson, J., Gillespie, J. and Mayne, M. (2008) uShuffle: a useful tool for shuffling biological sequences while preserving the k-let counts. *BMC Bioinformatics*, **9**, 192.
  24. Rot, G., Wang, Z., Huppertz, I., Modic, M., Lenče, T., Hallegger, M., Haberman, N., Curk, T., von Mering, C. and Ule, J. (2017) High-resolution RNA maps suggest common principles of splicing and polyadenylation regulation by TDP-43. *Cell Rep.*, **19**, 1056–1067.
  25. Patro, R., Duggal, G., Love, M.I., Irizarry, R.A. and Kingsford, C. (2017) Salmon provides fast and bias-aware quantification of transcript expression. *Nat. Methods*, **14**, 417–419.
  26. Lugowski, A., Nicholson, B. and Rissland, O.S. (2018) DRUID: a pipeline for transcriptome-wide measurements of mRNA stability. *RNA*, **24**, 623–632.
  27. Ricci, E.P., Kucukural, A., Cenik, C., Mercier, B.C., Singh, G., Heyer, E.E., Ashar-Patel, A., Peng, L. and Moore, M.J. (2014) Staufen1 senses overall transcript secondary structure to regulate translation. *Nat. Struct. Mol. Biol.*, **21**, 26–35.
  28. Knörlein, A., Sarnowski, C., de Vries, T., Stoltz, M., Götz, M., Aebersold, R., Allain, F.H.-T., Leitner, A. and Hall, J. (2022) Nucleotide-amino acid  $\pi$ -stacking interactions initiate photo cross-linking in RNA-protein complexes. *Nat. Commun.*, **13**, 2719.
  29. Ramos, A., Grünert, S., Adams, J., Micklem, D.R., Proctor, M.R., Freund, S., Bycroft, M., St Johnston, D. and Varani, G. (2000) RNA recognition by a Staufen double-stranded RNA-binding domain. *EMBO J.*, **19**, 997–1009.
  30. Cai, Z., Cao, C., Ji, L., Ye, R., Wang, D., Xia, C., Wang, S., Du, Z., Hu, N., Yu, X. *et al.* (2020) RIC-seq for global in situ profiling of RNA-RNA spatial interactions. *Nature*, **582**, 432–437.
  31. Laver, J.D., Li, X., Ancevicus, K., Westwood, J.T., Smibert, C.A., Morris, Q.D. and Lipshitz, H.D. (2013) Genome-wide analysis of Staufen-associated mRNAs identifies secondary structures that confer target specificity. *Nucleic Acids Res.*, **41**, 9438–9460.
  32. Lazzaretti, D., Bandholz-Cajamarca, L., Emmerich, C., Schaaf, K., Basquin, C., Irion, U. and Bono, F. (2018) The crystal structure of Staufen1 in complex with a physiological RNA sheds light on substrate selectivity. *Life Sci. Alliance*, **1**, e201800187.
  33. Bao, C., Zhu, M., Nykonchuk, I., Wakabayashi, H., Mathews, D.H. and Ermolenko, D.N. (2022) Specific length and structure rather than high thermodynamic stability enable regulatory mRNA stem-loops to pause translation. *Nat. Commun.*, **13**, 998.
  34. Dugré-Brisson, S., Elvira, G., Boulay, K., Chatel-Chaix, L., Moulard, A.J. and DesGroseillers, L. (2005) Interaction of Staufen1 with the 5' end of mRNA facilitates translation of these RNAs. *Nucleic Acids Res.*, **33**, 4797–4812.
  35. Calviello, L., Mukherjee, N., Wyler, E., Zauber, H., Hirsekorn, A., Selbach, M., Landthaler, M., Obermayer, B. and Ohler, U. (2016) Detecting actively translated open reading frames in ribosome profiling data. *Nat. Methods*, **13**, 165–170.
  36. Roy, B. and Jacobson, A. (2013) The intimate relationships of mRNA decay and translation. *Trends Genet.*, **29**, 691–699.
  37. Mayr, C. and Bartel, D.P. (2009) Widespread shortening of 3'UTRs by alternative cleavage and polyadenylation activates oncogenes in cancer cells. *Cell*, **138**, 673–684.
  38. Sandberg, R., Neilson, J.R., Sarma, A., Sharp, P.A. and Burge, C.B. (2008) Proliferating cells express mRNAs with shortened 3' untranslated regions and fewer microRNA target sites. *Science*, **320**, 1643–1647.
  39. Hogg, J.R. and Goff, S.P. (2010) Upf1 senses 3'UTR length to potentiate mRNA decay. *Cell*, **143**, 379–389.